Scientific Reports

https://doi.org/10.1038/s41598-026-44100-8

Article in Press

Wildfire fuel heat transfer sensor

Received: 17 November 2025

Accepted: 9 March 2026

Published online: 07 July 2026

Cite this article as: Marshall G.A., Linn R.R., Thompson D.K. *et al.* Wildfire fuel heat transfer sensor. *Sci Rep* (2026). https://doi.org/10.1038/s41598-026-44100-8

Ginny A. Marshall, Rodman R. Linn, Dan K. Thompson, Joseph J. O'Brien, Scott L. Goodrick & Arman Hemmati

Wildfire Fuel Heat Transfer Sensor

Ginny A. Marshall*[1,2], Rodman R. Linn[3], Dan K. Thompson[4], Joseph J. O'Brien[5], Scott L. Goodrick[5], and Arman Hemmati[2]

[1]Northern Forestry Centre, Natural Resources Canada, Edmonton, T6H 3S5, Canada
[2]University of Alberta, Mechanical Engineering, Edmonton, T6G 2R3, Canada
[3]Los Alamos National Laboratory, Earth and Environmental Science Division, Los Alamos, 87545, USA
[4]Great Lakes Forestry Centre, Natural Resources Canada, Sault Ste. Marie, P6B 2E5, Canada
[5]Southern Research Station, US Forest Service, GA, 30602, USA
*ginny.marshall@nrcan-rncan.gc.ca

ABSTRACT

Energy exchange in the fire environment is highly influenced by the heterogeneous and dynamic coupling between the atmosphere, fire, and fuels. While it has long been known that radiation and convection are the dominant heat transfer mechanisms in wildfire spread, much is unknown about their relative contribution. This is largely due to significant challenges observing these processes in the extreme wildfire environment. We describe a low cost, easy to deploy, simple heat transfer sensor and associated model, which was developed to measure heat transfer in wildfire. The sensor consists of stainless steel thermocouple probes differing in emissivity and similar in geometry and size to fine fuel elements responsible for carrying fire. Field and laboratory tests indicate that stainless steel probes with 3.2 mm and 1.6 mm diameters alone are not able to resolve the highly-dynamic heat transfer ahead of the fire. However, coupling the probes with a fine-wire thermocouple significantly improves its sensitivity. Results presented here indicate that the sensor and model are capable of measuring physically realistic convective and radiative heat transfer in high-intensity crown fire and simple laboratory scenarios when compared to observations in literature. Some limitations are identified for future investigation and additional testing and validation are required.

Introduction

Wildfire prediction and mitigation requires a comprehensive understanding of the driving processes that occur during wildfire, by which fuel elements ahead of the fire are heated, dried, and eventually combust. The rate of heat transfer between the fire front and the unburned fuel determines not only the ability of the fire to ignite and spread, but also the intensity of the fire[1]. In order to model wildfire behaviour, a thorough understanding of the driving mechanisms is required for development and corrections[2–5]. This involves direct measurements of energy transfer in wildfire[6], not only of the total energy transfer, but also of the individual components contributing to the total heat flux.

Heat transfer in wildfire occurs through conduction, convection, and radiation. Conduction, which can broadly be described as the transfer of kinetic energy by the collision of molecules, is most dominant within a solid or between solid fuel elements that are in contact with each other. The importance of conduction grows with the size of solid fuel elements or with the density of litter layers. Convection can be described as the transfer of heat through the bulk movement of a fluid. In the context of heat transfer to fuels in wildland fire, convection refers to the transfer of energy between a fluid and a solid which captures the effects of fluid motion in inducing a temperature gradient at the solid surface. This process makes convection more efficient than simple molecular conduction between the solid and the fluid. In the case of wildfire fuels, convection plays an important role as heated air warms cooler fuel elements in front of a fire, while ambient air is entrained over hotter fuel elements cooling them behind the fire. Convective heat transfer is heavily influenced by the magnitude of air velocity and its direction relative to the fire. Radiative heat transfer is the transfer of energy through electromagnetic radiation, which does not require a medium to carry energy. The magnitude of radiative heat transfer is a function of the temperature of emitting body. See Refs[7–9] for a comprehensive description of these processes.

It has long been known that the dominant heat transfer mechanisms in wildfire propagation are radiation and convection due to the dominant role of fine fuels in spread phenomena[1,10]. However, much is unknown about the relative contribution of convection and radiation due to difficulty of measuring their effects separately[6,11], particularly in wildfire fire scenarios. In recent years research has shown that convective heating, including that occurring in instances of direct contact by flame, is the most significant contributor for fire spread in fine fuels. Numerical simulations[12,13] and laboratory observations[14–17] suggest that in uniform fuel beds, preheating of the fine fuels by radiation is offset by convective cooling. Furthermore, ignition of the particles occurs only when the fuel is exposed to hot gases, including direct flame immersion or intermittent convective bursts related to buoyancy-induced instabilities. These exposures to hot gases momentarily eliminate the convective cooling and replaces it with strong convective heating that compounds the radiative heating[14,18–20]. Many laboratory studies have examined the relative role of these processes[15,17,21–25]; however, laboratory scale experiments are not always scalable to a wildfire environment[26]. Challenges in observing and documenting these processes in the field are numerous as instruments must withstand extreme temperatures, be self contained and portable, and be cost effective due to the high possibility of destruction[8,19,27]. As such, there are few field studies conducted to directly measure both modes of heat transfer during prescribed fire or wildfire[11,14,28–31]. The lack of field data not only limits our understanding of the roles of convection and radiation in a natural environment, but it also hinders our ability to validate wildfire behavior models that attempt to predict these critical processes[2]. Radiometers in the long-wave infrared, or thermal, spectrum are commonly utilized in field experiments to measure incident radiations. These systems typically consist of a bolometer or thermopile which is often located behind an external sapphire window to limit the influence of convective heating in measurements[8,28,32–34]. Measurements of fire radiation may be in-fire, or else on a fixed or overhead platform such as a tower or aircraft[35–37]. While radiation is relatively simple to measure, both observing and describing convective heat transfer is particularly challenging. First, it cannot be broadly described for a fire as it is very heterogeneous and it depends on the shape and size of fuel elements as well as air flow patterns in their immediate vicinity[6,8,9]. Convective heat transfer patterns are also extremely dynamic as the temporal scale of local velocity and temperature fluctuations are significantly less than 1 second. Moreover, they are determined by unsteady feedbacks between the evolving fire and surrounding atmosphere.

Given the difficulty in quantifying local velocity and temperature fluctuations for individual fuel elements, the majority of studies have examined the role of convection in a laboratory setting[6,25,31,38] or have employed combinations of total and radiant heat flux sensors or flat-plate thermometers to estimate convective heat transfer in wildfires. These sensors are well suited to withstand high-intensity wildland fires[28–30,39,40], as well as compartment fires or furnaces[41,42]. However, the geometry of these sensors—typically circular or square flat plates—is not representative of wildland fuel elements. Sensor geometry has a significant impact on heat transfer due to the formation of both velocity and thermal boundary layers along the fluid–sensor interface, which differ substantially between flow over flat plates and over cylinders or spheres. In natural settings, ignition and fire spread result from heat transfer to wildland fuels such as small twigs, needles, dry mosses, and dead grass, which are roughly cylindrical in shape. As a result, heat transfer estimates from previous work, particularly for convective heat transfer, may not accurately reflect the processes occurring in fuels that sustain and spread fire. Other studies have acknowledged the importance of geometry in heat transfer by employing sensor shapes that mimic vegetative structures, such as buds[43].

In an effort to develop easily deployable instruments that can tolerate extreme environments in wildfire, the United States Department of Agriculture's Forest Service developed a Fire Behavior Package and a Heat Transfer Package in their Missoula Fire Lab. The Fire Behavior Package[19,44] contains two flow sensors, one oriented vertically and one oriented horizontally, measuring wind with up to 50–60° in different directions. It also contains a thermocouple, a narrow angle radiometer, and heat flux sensor to capture wide angle radiation and total heat flux. The combination of these sensors allows for determining convective and radiation components of heating to items with geometries of these instruments. The Heat Transfer Package[27] was developed to improve the observation capability of the system with respect to wind directionality and temporal sampling by employing disk anemometers. However, these packages are complex and require sophisticated electronics and construction.

In this work, we describe a simple wildfire Fuel Heat Transfer Sensor[45] designed for measuring in-fire radiation and convection induced heat transfer along with preliminary measurements. We note that this is not a thorough validation of the sensor, but a demonstration of proof of concept and a comparison to data observed in similar fires. The sensor requires rigorous testing across the entire range of fire intensity observed in wildfires, which we leave for future work.

Methods

The following section describes the theory behind our wildfire Heat Transfer Sensor, the physical description of the sensors, and the experiments designed to test their performance.

Theory

The thermal energy change in wildland fuels, before the arrival of flames and initiation of the combustion process, is largely influenced by radiative and convective heating and cooling, as well as conduction (or thermal diffusion) within thick fuels or between smaller fuel elements. This evolution is described by Equation 1, where the left hand side describes time-rate-of-change in internal energy of the fuel, and terms on the right hand side (from left to right) represent radiative heating, radiative cooling, convective heat transfer, and thermal diffusion:

$$\frac{\partial c_p m_f T_f}{\partial t} = E\frac{A}{\pi}\varepsilon_f - A\sigma\varepsilon_f T_f^4 + hA\left(T_{air} - T_f\right) + \frac{\partial}{\partial x_i}\left[\kappa\frac{\partial T_f}{\partial x_i}\right]. \tag{1}$$

Here, T_f, c_p, and m_f are temperature, specific heat capacity and mass of the fuel element, respectively, while t is time, E is the incident radiation flux to the fuel element, A is surface area, $\frac{A}{\pi}$ is surface area exposed to incident radiation if we assume the fire front approaches the probe from one direction, ε_f is emissivity, σ is the Stefan-Boltzmann constant, h is the convective heat transfer coefficient, T_{air} is air temperature, x_i represents the spatial direction, and κ is thermal diffusivity for the fuel element. In this energy balance, we assume a cylindrical fuel element with emissive energy loss and convective energy exchange occurring over the entire integrated surface. However, in a likely scenario, a fire front approaches a fuel element from one direction, which is the projected area, or $\frac{A}{\pi}$. Following Kirchhoff's Law, we assume that ε_f is the same in both radiation gain and loss terms, such that absorptivity is equal to emissivity. Here we assume the probe is in thermal equilibrium with its surroundings.

Ignition typically occurs in smaller fuel elements first, as moisture is easier to drive off and a given heat flux raises the temperature of the thinner elements faster than thicker elements. Moreover, larger fuels have more thermal mass, which moves energy away from the surface by conduction. Since we are primarily interested in fast burning fuels that carry the flame front, rather than thermally-thick fuels that tend to ignite slowly and have lower heat release rates per-unit-mass, we consider Equation 1 only for thermally thin fuels, where thermal gradients are not sustained. Thus, we apply a small Biot number approximation (the dimensionless number relating the internal resistance to conduction to the external or surface, resistance to convection) allowing us to neglect the thermal diffusion term on the right had side of Equation 1 and arrive at

$$\frac{\partial c_p m_f T_f}{\partial t} = \frac{A}{\pi} E \varepsilon_f - \sigma A \varepsilon_f T_f^4 + hA\left(T_{air} - T_f\right). \tag{2}$$

As a result, we have an equation for time rate of change of the internal energy of fine fuel element (or a surrogate object like thin wire for example) as a function of only radiation and convection. Given a fuel element with a known mass, specific heat capacity, surface area, emissivity, and a measured temperature, the only unknown terms in the above equation are incident radiation, the convective heat transfer coefficient, and air temperature. If we can simultaneously measure temperature in three elements with different emissivities situated close enough to each other that they are all exposed to the same local conditions, we can derive a system of equations using Equation 2 to solve for the unknown radiative and convective heat transfer of the system. Furthermore, if we can measure the local air temperature, only two fuel elements are required.

Following the design outlined in the Forest Fire Fuel Heat Transfer Sensor patent[45], we describe several possible configurations of a sensor that consists of thermocouple probes with different, but known, emissivities. The purpose of the proposed sensor is to measure incident radiation and convective heat transfer to fine fuels in wildfire applications using a robust, cost effective, and easy to deploy system.

Sensor Description: 3-Probes

The sensor consists of three stainless steel thermocouples probes[45] that act as surrogates for fine fuels (with similar geometry, and thus, convective heat transfer coefficient), which are convenient for measurement purposes. Each probe has a different surface treatment and thus a different emissivity/absorbtivity. Since the specific heat capacity, mass, temperature, surface area, and emissivity of each probes is known or easily measured, we can utilize Equation 2 to generate a system of three equations (one for each probe) with three unknowns: incident radiation, E, convective heat transfer coefficient, h, and air temperature, T_{air}. Since the probes have the same geometry and are located in close proximity of one another, we can assume (given a large enough heat source relative to this spacing) that all probes are exposed to the same incident radiation, and all have the same local air temperature and air velocity (and thus the same convective heat transfer coefficient). Therefore, determining incident radiation and convective heat transfer is a simple algebraic exercise.

Beginning with convective heat transfer coefficient for the system, we rearrange Equation 2 for each of the three probes, such that

$$\frac{E\varepsilon_i}{\pi} + h\left(T_{air} - T_i\right) = D_i = \frac{c_p m_i}{A}\frac{\partial T_i}{\partial t} + \sigma \varepsilon_i T_i^4, \tag{3}$$

where subscripts $i = 1,2$ or 3, one for each probe, and D_i is the internal energy rate of change plus the radiated energy of each probe per-unit-area. The mass and specific heat capacity of stainless steal probes will not change with time, and thus we can solve for the time rate of change in temperature using an explicit approximation:

$$\frac{\partial T_i}{\partial t} = \frac{T_i(t + \Delta t) - T_i(t)}{\Delta t} \tag{4}$$

where Δt is the time step between measurements. If we subtract Equation 3 for probe 1 from the equivalent Equation for probe 2, we arrive at

$$D_2 - D_1 = \frac{E}{\pi}\left(\varepsilon_2 - \varepsilon_1\right) + h\left(T_1 - T_2\right) \tag{5}$$

which contains two of the three unknowns, h and E. The remaining values we can directly measure or calculate using the thermocouple probes. The convective heat transfer coefficient value is often approximated using empirical methods, where it is associated with the Nusselt number, Nu, under forced convection. The Nusselt number is defined as the ratio between convective heat transfer and conductive heat transfer,

$$Nu = \frac{hL}{\kappa}, \tag{6}$$

where L is the relevant length scale (diameter of the probe in this case) and κ is thermal conductivity of the fluid. The Nusselt number can be empirically represented as a function of the local Reynolds number, Re, which characterizes the local flow, and Prandtl number, Pr, which is the ratio of energy transfer via momentum to thermal energy transfer:

$$Nu = CRe^m Pr^n. \tag{7}$$

Combining Equations 6 and 7, the convective heat transfer coefficient for small cylindrical shaped fuel elements (e.g. needles, grasses, fine branches) or the stainless steel probes (surrogate fuel element) can be then estimated[46] as

$$h = \frac{0.683\kappa_f Re^{0.466} Pr^{0.333}}{L}, \tag{8}$$

where $C = 0.683$, κ_f is thermal conductivity of air in the vicinity of the fuel particle. The Prandtl number in air does not change appreciably over environmental temperatures and is often assigned a value of 0.7[29,47,48]. The Reynold number is calculated as

$$Re = \frac{UL}{\nu} \tag{9}$$

where U is local flow speed, and ν is kinematic viscosity of the fluid. Rather than measuring local flow parameters required to calculate the convective heat transfer coefficient directly, which is extremely challenging during wildfire, we propose rearranging Equation 5 to arrive at:

$$h = \frac{(D_1 - D_2) + \frac{E}{\pi}(\varepsilon_2 - \varepsilon_1)}{(T_2 - T_1)}, \tag{10}$$

which requires the unknown incident radiative flux, E. It should be acknowledged that we can not use this form of the equation to solve for h if the gas and the probe temperatures are the same. So for practical use, the convective heat transfer term can be neglected from Equation 5 when the temperatures of the probes and gas temperatures are sufficiently close.

By repeating a similar process with Equation 3 and subtracting the equivalent Equation for probe 1 from probe 3 to solve for E, we get:

$$E = \pi \frac{(D_3 - D_1) + h(T_3 - T_1)}{(\varepsilon_3 - \varepsilon_1)}. \tag{11}$$

We can then substitute Equation 11 into Equation 10 and after rearranging, we arrive at

$$h = \frac{(D_1 - D_2)(\varepsilon_3 - \varepsilon_1) + (D_3 - D_1)(\varepsilon_2 - \varepsilon_1)}{(T_2 - T_1)(\varepsilon_3 - \varepsilon_1) + (T_1 - T_3)(\varepsilon_2 - \varepsilon_1)} \tag{12}$$

which contains only variables that are known or measured. It should be recognized that in dynamic heating/cooling scenarios it is possible the denominator in Equation 12 can be zero momentarily when all probe temperatures are the same, or when $(T_2 - T_1)(\varepsilon_3 - \varepsilon_1) = -(T_1 - T_3)(\varepsilon_2 - \varepsilon_1)$.

To determine the incident radiative heat received by the probes, we rearrange Equation 10 and solve for E using the calculated heat transfer coefficient from Equation 12. Then, the incident radiative heat transfer per-unit-area is determined:

$$Q_{rad,i} = \frac{E\varepsilon_i}{\pi}, \tag{13}$$

assuming exposure is from one direction. To determine the convective heat flux, we next need to solve for air temperature. Rearranging Equation 3 for probe 1, we arrive at

$$T_{air} = \frac{D_1 - \frac{E}{\pi}\varepsilon_1}{h} + T_1. \tag{14}$$

Air temperature calculated using each probe may vary due to measurement or approximation errors, thus it is recommended to calculate it using the average of all three probes.

Finally, the convective heat transfer and emitted energy per-unit-area for each probe can be solved as:

$$Q_{conv,i} = h\left(T_{air} - T_i\right), \tag{15}$$

and

$$Q_{emit,i} = \sigma \varepsilon_i T_i^4, \tag{16}$$

where $Q_{conv,i}$ is the convective heat exchange and $Q_{emit,i}$ is the radiative loss in each probe.

Sensor Description: 2-Probes

The model described above can be reduced to a 2-probe system when gas temperature can be measured directly. Probes with significantly different emissivities in the mid- and long-wave infrared spectrum are most appropriate[45], i.e., a near black probe and a highly-polished probe. Applying Equation 3 for probes 1 and 2 and eliminating the unknown incident radiation E, we arrive at a new equation for the convective heat transfer coefficient in the 2-probe variation,

$$h = \frac{D_1\varepsilon_2 - D_2\varepsilon_1}{\varepsilon_2\left(T_{air} - T_1\right) - \varepsilon_1\left(T_{air} - T_2\right)}. \tag{17}$$

Similarly, we can eliminate h instead and arrive at another expression for incident radiation,

$$E = \pi\frac{D_1\left(T_{air} - T_2\right) - D_2\left(T_{air} - T_1\right)}{\varepsilon_1\left(T_{air} - T_2\right) - \varepsilon_2\left(T_{air} - T_1\right)}. \tag{18}$$

We note that the denominator in both Equations 17 and 18 become zero momentarily when $\varepsilon_2\left(T_{air} - T_1\right) = \varepsilon_1\left(T_{air} - T_2\right)$. In such cases, h and E become undefined. Once the values of h and E are determined, radiative and convective heat fluxes to the probes can be determined using Equations 13 and 15.

Experimental Design

The following section describes the sensor design and provides an overview of the initial field and laboratory tests.

Sensors

The sensors were custom built to withstand high-intensity wildfire based on patent description by Linn *et al.*[45]. The sensor box dimensions are 15.2 cm× 15.2 cm × 11.4 cm, and it is constructed with 1.6 mm thick steel. The box is insulated with 25 mm calcium silicate thermal insulation, which is then lined with a foil faced fiberglass cloth. Fiberglass insulated, 24 AWG (American Wire Gauge), K-type thermocouple wire with Inconel overbraiding is threaded through steel conduit connecting a data logger to mini ceramic connectors. The ceramic connectors are held in place by custom metal housing and the insulated lid exposes the majority of the thermocouple probes, while shielding the ceramic connectors from excessive heat.

The configuration shown in Figure 1 consists of three 3.175 mm (0.125 in) wide, 152.4 mm (6 in) long, tip-grounded, K-type thermocouple probes (Dwyer Omega) spaced 25.4 mm apart. The length of the probes within the insulated box is approximately 13 mm. One probe is sprayed black with Rust-Oleum Specialty High Heat spray paint in a flat finish, another is polished with Sharpal green buffing compound, and the last is sandblasted to a dull finish with 80 grit aluminum oxide blasting compound. The emissivities, ε_i, of the probes are 0.9, 0.3 and 0.1 for the black, dull, and silver (or polished) probes respectively. Emissivities are rounded to the nearest one tenth due to uncertainty and potential inconsistencies in probes. These values were estimated using a combination of thermal camera observations, published values, and sensitivity testing. Thermal images of the probes were combined with the known thermocouple temperature and the Stefan-Boltzmann equation to determine emissivity. Estimates were also cross-referenced with published values[49–52]. Black spray paint is reported 0.85–0.98, sandblasted stainless steel 0.38, and polished stainless steel 0.07– 0.3 in extreme temperatures.

(a) (b)

Figure 1. Images of the sensor (a) installed and (b) a close up of the probes

Conductive loss in the probe above the ceramic connectors is considered negligible as less than 15 mm (<10%) of the probe is shielded by insulation. If we assume the cross-sectional area of the hollow probe is $A_c \approx 5.938 \times 10^{-6}$ m^2 (the hollow radius is half the outer radius), then conductive loss can be calculated as:

$$Q_{conduct} = \frac{\kappa_{steel} A_c \left(T_f - T_{insulated}\right),}{L} \tag{19}$$

where κ_{steel} is thermal conductivity of stainless steel, taken to be 15 Js^{-1}m^{-1}K^{-1}, $T_{insulated}$ is the probe temperature at the ceramic connector, and L is the 15 mm length over which the probe is conducting heat away. Assuming an extreme (and unrealistic) temperature difference of 900 K, the energy loss over 1 second would be approximately 5 J. While this loss will compound over time, the energy gains due to fire-induced convection and radiation are expected to be at least an order of magnitude larger for even the lowest intensity fires, which would have significantly smaller temperature difference. Thus, we neglect conductive losses for these applications.

Field Tests

An experimental fire was conducted by the Government of the Northwest Territories Environment and Climate Change on June 24, 2025 at the Fort Providence Wildfire Experimental Site[53], formerly the location of the International Crown Fire Modeling Experiment[54]. The stand at the plot was primarily black spruce and jack pine with nearly 80% of the jack pine overstory standing dead. Understory consisted of primarily black spruce with aspen, birch, and jack pine. Surface fuels were a mixture of feather moss and shrubs. The sensor was installed approximately 50 m north of the ignition line expecting northward fire spread. In-stand winds at 1.5 m above ground level (AGL) and 30 m upwind of the ignition line were approximately 0.6 ms^{-1} at ignition time. 10 meter open winds were between 1.8 and 2.0 ms^{-1} during the fire. Temperature and relative humidity at 2 m were 22°C and 34%. The Canadian Fire Weather Index System's[55] Fine Fuel Moisture Code (FFMC), Duff Moisture Code (DMC), Drought Code (DC), and Fire Weather Index (FWI) were reported as 91, 77, 327, and 27, respectively. These conditions in a boreal spruce stand were conducive to continuous crown fire. Further details on the experimental fire will be reported in additional studies.

The sensor was carefully buried such that the tip of the probes were approximately 8 cm above the moss and litter layer, see Figure 1a. This height ensured that the thermocouple junction was near the surface, but not below the moss layer. Air temperatures at the plot were measured in multiple locations using K-type fine wire thermocouples, 36 gauge, or 0.127 mm in diameter, connected to 24 AWG, fiberglass insulated thermocouple wire with a stainless steel overbraid. The fine wire thermocouple and insulated thermocouple wire were connected with a bead of silver brazing alloy.

Air temperature measurements were logged at multiple locations near the sensor at 1 Hz using a Campbell Scientific CR1000 datalogger and thermocouple probe measurements were logged at 1 Hz with a Campbell Scientific CR800 datalogger. We report air temperatures as measured by the fine-wire thermocouples, without correction for radiation. Following other studies[11,29,40,56] we estimate the error to be 5% since the fine-wire thermocouples are 0.127 mm. Temperature errors and their impacts on results are further discussed in Supplementary Material. All loggers and batteries were buried in a logger box 1 m west of the sensor. Surface fuels upwind of the sensors were undisturbed and fuels in adjacent areas were minimally disturbed, except above the buried data loggers, where all fuel was removed and 10 cm of wet clay was overlaid to protect the loggers and batteries from excessive heat.

In the 2-probe calculations, T_{air} is the mean air temperature of the west, central and east fine-wire thermocouples which were located approximately 10 cm south of and no more than 50 cm east / west of the probes. Analysis of near-surface air temperature data within 100 cm upwind of the sensor generally follows the trends of that observed 50 cm upwind and laterally. This indicates well mixed gas temperatures in the 1 m region near the probes, and thus the mean value from west, central and east locations are likely representative of local gas temperatures. We use only the black and polished probes to maximize the difference in emissivities, as recommended in the patent[45]. The time rate of temperature change (required in Equation 3) for each probe was calculated using the slope from the line of best fit for the data between two seconds prior and two seconds following each sampled temperature.

Laboratory Tests

To examine the potential influence of probe thickness or their response time scales, simple laboratory test fire experiments were performed with two different size probes (3.175 mm and 1.588 mm in diameter) in dead grass, primarily *Elymus trachycaulus* and *Bromis inermis*. Calm and wind (driven by a fan) cases were tested. In the wind case, the wind speed at the level of the probes was approximately 1.4 ms^{-1}. In all laboratory tests, 150 g of grass was evenly spread over a surface of calcium silicate thermal insulation approximately 1 m long and 0.5 m wide resulting in an average fuel load of 0.3 kg m^{-2} with a depth of approximately 6 cm, similar to a matted dead grass after spring thaw. The thermal insulation was installed to ensure energy from the fire was not reflected back into the fuel bed. Fuel moisture was 10% for both tests (with and without wind). The sensors were placed in the fuel bed with probes oriented vertically, in a line parallel to the ignition line, laterally centred in the fuel bed, and located approximately 5–10 cm in from the far edge (and 95 cm from the ignition line). The probes were positioned 10 mm apart (centre to centre) to accommodate the size of the fuel bed, which differs from the probe spacing of 25.4 mm described for the sensor box assembly. Ignition occurred along the edge opposite the sensors and the fire was allowed to freely burn to the probes. The sensors were also collocated with two 0.127 mm fine wire thermocouples to measure gas temperature within 2 cm of the probes. For all laboratory tests, a single CR1000 data logger was used to record temperatures of both the probes and fine-wire thermocouples at 1 Hz.

Numerical tests

We examine the time sensitivity of the probes using a forward in time discretization of the conduction equation,

$$\frac{\partial c_p m_f T_f}{\partial t} = + \frac{\partial}{\partial x_i}\left[\kappa \frac{\partial T_f}{\partial x_i}\right] \tag{20}$$

with 21 grid cells, and a time step of 1×10^{-4} s. In this numerical analysis, the probe is assumed solid across the entire width, the heating is assumed to be antisymmetric, thermal diffusivity is a function of the local temperature, and cylindrical influences of the probe shape were ignored. Mass and specific heat capacity are assumed constant. A Dirichlet boundary condition was applied on one side assuming temperature symmetry across the centre of the probe and a Neumann boundary condition on the edge representing the exterior of the probe. A constant initial temperature, T_i, of 300 K is assumed and a boundary condition of $T_i + 100$, $T_i + 200$, $T_i + 300$ were applied to ensure consistency.

Results and Discussion

The following section illustrates data from the initial field test, two laboratory tests, and discussion of the results.

Field Tests

The sensor was tested near Fort Providence, Canada on July 24, 2025. The fire in the immediate vicinity of the test plot was a high-intensity crown fire with a residence time of approximately 60 s as determined by in-fire video and near surface air temperatures. Figure 2 illustrates measured temperatures from the probes and fine wire thermocouples. Subscripts $Air,west$, $Air,centre$, and $Air,east$ correspond to air temperatures measured west, immediately upwind, and east of the sensor. Air,avg is the average of the three. Prior to arrival of the flame front, a spot fire ignited near the sensor which is evident after 50 s in

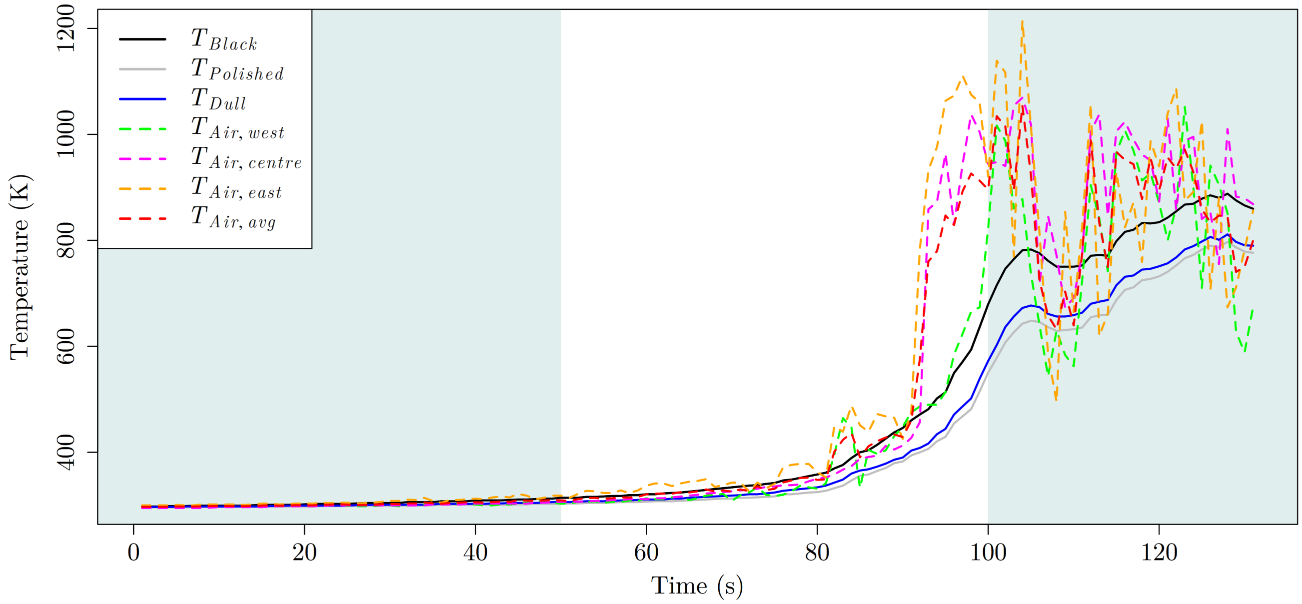

Figure 2. Near ground probe and air temperature measurements before and during fire front arrival for the field experiment conducted near Fort Providence, Canada. 0 s roughly corresponds to the point in time where the temperatures begin to slowly rise above ambient as the fire front approaches. Grey-green shading on the background of the plot indicates time periods where data is not discussed in the analysis below, but is shown here for completeness.

$T_{Air,east}$ in Figure 2 and visible in Figure 3a within the blue box. The spot fire has minimal effect on the sensor as the probe temperatures remain near the $T_{Air,centre}$ and $T_{Air,west}$ until the flame front approaches. At approximately 82 s, a gust of hot gases is evident in $T_{Air,east}$ and $T_{Air,west}$ with a brief increase between 125 and 135 K before the arrival of the fire front. $T_{Air,centre}$ does not rise at the same magnitude as $T_{Air,west}$ and $T_{Air,east}$, possibly due to brief contact with fuel, such as a leaf blown in. The brief gust of hot gases and associated convection has minor impact on the temperature evolution of the probes. Examination of the first time derivative (not shown for brevity) of probe temperatures over time shows an elevated time rate of change of temperature starting just before 82 s, increasing between 5.4 and 6.0 Ks^{-1}, followed by a momentary decline until rising between 7 and 38 Ks^{-1} with the approach of the fire front (90–100 s). Upon the arrival of the fire front around 92 s, $T_{Air,west}$ rise lags behind $T_{Air,centre}$ and $T_{Air,east}$ by approximately 7 s as shown in Figure 2. In-fire images (Figure 3) indicates that while stand-level direction of fire spread is south to north, the fire locally approached the sensors from the east due to spot fires on the eastern side of the sensors, as well as erratic and turbulent flow at the fire front. Moreover, this local behaviour of the fire may be influenced by the fallen tree (visible) and clay fuel break protecting the buried loggers (not visible). It is worth noting the metal frames in Figure 3 are placed to support fine-wire thermocouples. The sensor described here (located within the blue box in Figure 3a) is positioned near the north frame to utilize measured near-ground air temperature.

In order to explore the performance of the proposed sensor, we must consider that soot accumulation and oxidation will change their emissivities, and thus we cannot assess the performance of the system after the probes are engulfed in flame. This is a known challenge during in-fire measurements[28,33,57]. Assessments of probe emissivity evolution due to oxidation, thermal degradation, and soot accumulation during and post-flaming are required to determine the applicability of the sensor during flame contact. This work is left for future studies. Furthermore, analysis is irrelevant when probe and gas temperatures are nearly identical to each other since there is little to no fire-induced heat transfer. Therefore, we only discuss results between 50–100 s in our analysis hereafter and exclude all other data (shown as light grey-green shading in Figure 2).

Calculated heat transfer coefficients for the interval of relevance are plotted in Figure 4a and incident radiations in Figure 4b. Here, $h_{3-probe}$, $h_{2-probe}$, and $h_{2-smoothed}$ are the calculated convective heat transfer coefficients for the 3-probe system, 2-probe configuration, and smoothing of $h_{2-probe}$, respectively. $E_{2-probe}$ and $E_{3-probe}$ are incident radiation calculated from the 2- and 3-probe systems.

We begin by noting the surprisingly-large fluctuations in both the convective heat transfer coefficient and the incident radiation in the 3-probe system, as well as the tendency for both to fall below zero. The convective heat transfer coefficient itself is a measure of how well heat can be transferred between a surface and the surrounding fluid in the direction opposing

(a) (b)

Figure 3. Still images from in-fire video (a) before the arrival of the fire front while a spot fire ignited near the sensor, and (b) as the flame front initially arrives. The blue box in (a) contains both the spot fire and sensor. The camera is pointed approximately east. Photo Credit: Greg Baxter, FPInnovations

the temperature gradient (hot to cold). Larger values of h indicate more efficient heat transfer, and values near 0 indicate negligible heat transfer. Furthermore, a negative coefficient would indicate the transport of heat from cold mass to hot mass, which is unphysical. An examination of $h_{3-probe}$ in Figure 4a indicates a frequent mismatch between the sign of the numerator and denominator in Equation 12. While the signs for each individual term are physically realistic and consistent (e.g., $(D_1 - D_2)(\varepsilon_3 - \varepsilon_1) < 0$) the accuracy and response time of the 3.175 mm probes for the 3-probe configuration is not sufficient to determine the convective heat transfer coefficient in a rapidly changing energy balance. Calculation of the coefficient depends on the highly-dynamic temperatures of the probes, which are not adequately captured by the probes at the time scale changes of velocities, density, and temperatures of the gases around the probes. In order to explore the potential challenges associated with the time scales of probe response, we used a simple 1 dimensional conduction model in an ideal 3.175 mm wide probe. Results indicate that it takes approximately 2.1 s for the centre of the probe to reach 90% of the applied temperature on the edge of the probe. Temporal fluctuations in convective heat flux up to 200 Hz for 2.2 ms^{-1} are observed in wind driven laboratory experiments[23].

While we are unable to measure the heat transfer coefficient directly for validation, we can assess its relative accuracy using Equation 8 and comparison to literature. For example, we expect a low convective heat transfer coefficient (<10 Wm^{-2}K^{-1}) in low winds (e.g., 0.1 ms^{-1}), although natural convection will prevent it from going to zero if there is a temperature difference between the probe and surrounding air as buoyancy-induced velocities will develop. The coefficient rises to 175 Wm^{-2}K^{-1} as air temperatures and winds rise to 600 K and 10 ms^{-1}, and approaches 240 Wm^{-2}K^{-1} in air at 1000 K with 20 ms^{-1} winds. Video observations of the experimental fire indicate continuous, and at times extreme, swaying of trees several meters tall and several centimetres in diameter with the approaching fire front; thus, it is reasonable to assume local near ground fire-influenced wind speeds are nearing and exceeding 10 ms^{-1}. Horizontal in-fire winds, as reported[58] in a high-intensity crown fire were estimated to be 5–15 ms^{-1} in a denser stand at the Fort Providence site. Moreover, a high-intensity fire in Alaska[59] generated horizontal winds of 10 ms^{-1} with peaks of 30 ms^{-1}. Wind speeds up to 16.2 ms^{-1} were reported[11] in a surface fire with flames extending into the canopy.

In Figure 4a, the heat transfer coefficient for the 2-probe system varies (generally) between 40 and 110 Wm^{-2}K^{-1} from 50–70 s, and fluctuating as high as 362 Wm^{-2}K^{-1}. Smoothing the calculated 2-probe heat transfer coefficient between 50–100 s yields an initial mean value near 75 Wm^{-2}K^{-1} that rises to approximately 240. The smoothed line presented in Figure 4a is generated using LOESS curve-fitting with span of 0.4 that is fitted using data within the interval 50–100 s, which explains the local minima at approximately 95 s. While the probes themselves cannot resolve rapid fluctuations in convective heat transfer, the fine-wire thermocouple sensitivity is significantly better, resulting in an increase in overall performance of the 2-probe variation.

Figure 4b illustrates the calculated incident radiation received by both the 2- and 3-probe systems in the experimental fire. Since we separate the incident and emitted thermal radiation in our model, negative calculated values for E in the 3-probe system are nonphysical. Such values are likely due to the inability of the system to resolve the convective heat transfer accurately. Instead, incident radiation is more realistic using the 2-probe system, where fluctuations in gas temperature are better accounted for. In the 2-probe system, incident radiation increases with decreasing distance to the fire front, which is consistent with other studies. The peak incident radiation observed just prior to flame arrival is approximately 200 kWm^{-2}, which is similar to

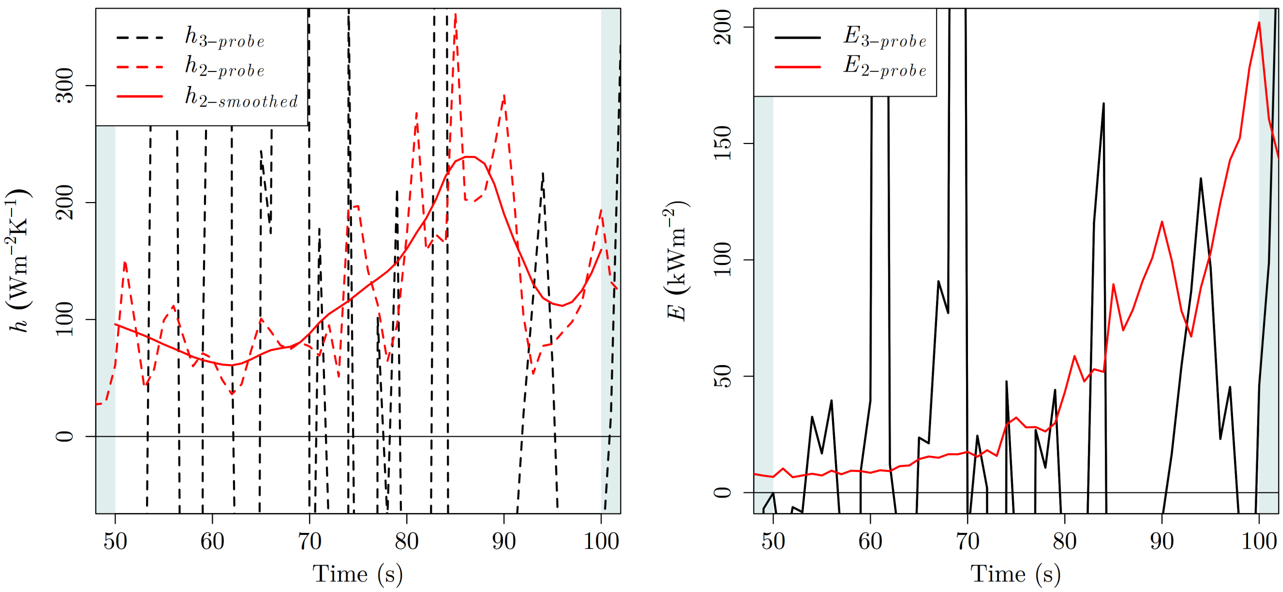

(a) **(b)**

Figure 4. Calculated (a) convective heat transfer coefficient, *h*, and (b) incident radiation, *E*, for both the 2-probe and 3-probe system.

the peak of 189 kWm^{-2} observed in Mill Creek crown fire[33]. Other studies in high-intensity crown fire have reported values of radiant heat fluxes peaking near 200 kWm^{-2} at 3 m AGL[30] and 300 kWm^{-2} at 1 m AGL[33]. Studies in shrublands and in passive crown fire report peaks greater than 150 kWm^{-2} near the vegetation tops (1.1 m AGL)[40] and up to 52 kWm^{-2} at 0.6 m AGL[11] . It is important to recognize that the local site conditions for all of these studies will vary significantly and the radiant energy fluxes discussed above are to establish a plausible range of values in moderate- to high-intensity fire. In the sensor described here we may not accurately capture the maximum radiative flux because it can occur while the probes are fully engulfed in flame and thus becoming soot coated (changing emissivity values of the probes). Furthermore, very short duration spikes are likely smeared out by the time-scale resolution of the probes since measurements less than 10 Hz are unlikely to capture peak fluxes[39]. Nonetheless, the sensor is reporting physically realistic results falling within the range of radiant heat fluxes reported by other studies in moderate- to high-intensity fire.

We report the final energy budget calculated using only the 2-probe system in Figure 5. In this figure, the black probe budget is presented with black lines and the polished probe results are presented in grey. Beginning with the convective heat transfer per-unit-area from Equation 15, the calculated polished probe convective energy is positive during the approach of the fire front as the temperature of the probe never rises above the temperature of the air. The black probe, however, has brief periods of convective energy loss lasting from 1 s to5 s with the approaching fire front. This pattern of alternating positive and negative convective heat transfer is consistent with laboratory observations[14]. Pre-ignition, fuels are being heated steadily by incident radiation, raising the probe temperature, while intermittent bursts of hot and cooler gases heat and cool fuel particles. The greatest convective energy received is by the polished probe around 98 s, at or momentarily before flame impingement. The fact that convective heat transfer in the polished probes is always positive highlights the important role that incident radiation plays in pre-heating fuels. Unlike the black probe, the polished probe reflects 90 % of incident radiation leading to heating primarily by convection. However, convective cooling is expected in natural fuel elements[16] that absorb a significant portion of incident radiation[60,61].

The incident radiative energy absorbed (Equation 13) is significantly different in the black and polished probes, which is due to differences in emissivity as the polished probe reflects much more energy than the black probe. As expected, the radiative energy for the black probe rises steadily as the fire front approaches, and it is strongest just before or at flame contact when convective heat transfer is nearly as strong. Finally, the emitted energy, or radiative energy losses, by the probes (Equation 16) are most significant in the black probe and near 0 for the polished probe.

Considering that emissivities of live and dead vegetation are often above 0.9[60,61], and the geometries of the natural fuel elements and probes are similar, the energy absorbed or lost in the black probe would be comparable to that of the fine fuel

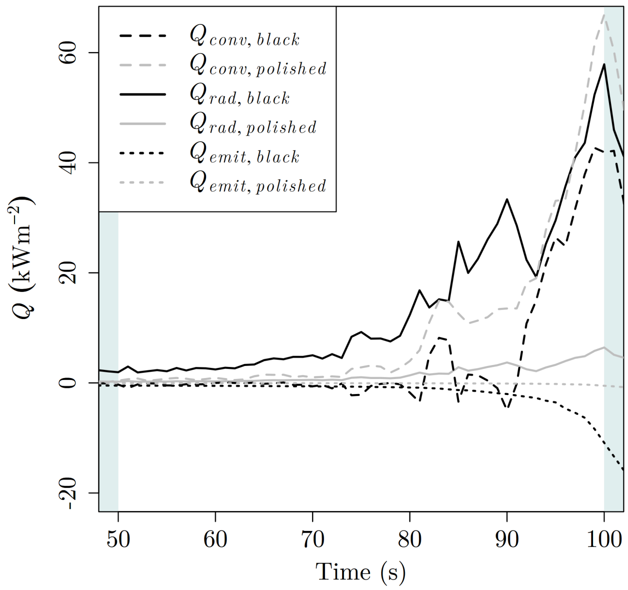

Figure 5. Energy budget for the sensor probes during the experimental fire. Convective heat transfer flux is Q_{conv}, the radiative flux is Q_{rad} and the emitted energy from radiation loss is Q_{emit}.

elements which carry fire in a natural setting, recognizing there are significant differences in specific heat capacities and moisture dynamics. The pattern of generally increasing radiative heating with decreasing distance to the fire front and bursts of convective heating and cooling prior to flame contact are consistent with numerically-motivated hypothesis[12,13] and physical findings[14,33,62]. Furthermore, observations that incident radiation may contribute more energy per-unit-area than convective heat transfer, which can and does induce cooling in high-intensity crown fire, is consistent with some other studies[33,62] that report average peak convective heat fluxes near 45%[33] and 15–20%[62] of the incident radiation in lodgepole pine stands. In this investigation, we observe 22%, recognizing that difference in geometries of the instruments make direct comparison difficult. Nonetheless, this initial investigation of the performance of the sensor (when gas temperature is measured) is promising. The time scales of the 3 mm probes are not adequate to resolve rapid changes is convective heat transfer. While we originally sample at 1 Hz, we estimate the probes cannot resolve fluctuations smaller than 4-5 seconds. In addition to the numerical analysis, shortening the duration for the time derivative (currently ± 2 s) shows no improvement in results, and averaging of the data on a 5 second moving window indicates very similar trends, with less variation. Following these findings, we attempt to improve the sensitivity of the system by reducing the probe size as described in the next subsection. To date, there is no experimental fire data for the smaller probes.

Laboratory Tests

Several laboratory tests were conducted at the Northern Forestry Centre in Edmonton, Alberta, Canada to assess possible improvements in sensitivity of the 2- and 3-probe systems by comparing their performance against a similar set of thermocouple probes with a smaller diameter. This section presents the results and discussion on a calm case and a case where wind (using a fan) was applied.

Figure 6 illustrates temperature observations for the small and large probe comparison in (a) calm (no wind) scenario, and (b) 1.4 ms^{-1} wind scenario. The mean air temperature in these plots, $T_{Air_{avg}}$, is measured within 2 cm ahead of each set of probes. Examining the temperature trends, we note the slow temperature rise of the probes in the absence of wind. Both gas and probe temperatures initially are slow to rise, with a sharp rise in gas temperature at 63 s, followed by a slower rise in both small and large probes. Finally, a notable increase in probe temperatures occurs at 75 s where the flames are in direct contact with the sensor. This is contrasted in the wind scenario, where the gas temperatures rises rapidly at 24 s, followed by a notable rise in all probe temperatures at 26 s. The greatest increases are observed in the smaller probes.

Examining the heat transfer coefficient for both calm and wind scenarios in Figures 7a and 7b, large positive and negative fluctuations occur again in the 3-probe system. Therefore, the remaining discussion will focus on only 2-probe variations. The heat transfer coefficient for the 2-probe scenario in no wind is very small in both size systems with a mean (peak) of 9 (45) Wm^{-2}K^{-1} and 11 (28) Wm^{-2}K^{-1} for the large and small systems, respectively. We note the larger probes illustrate negative

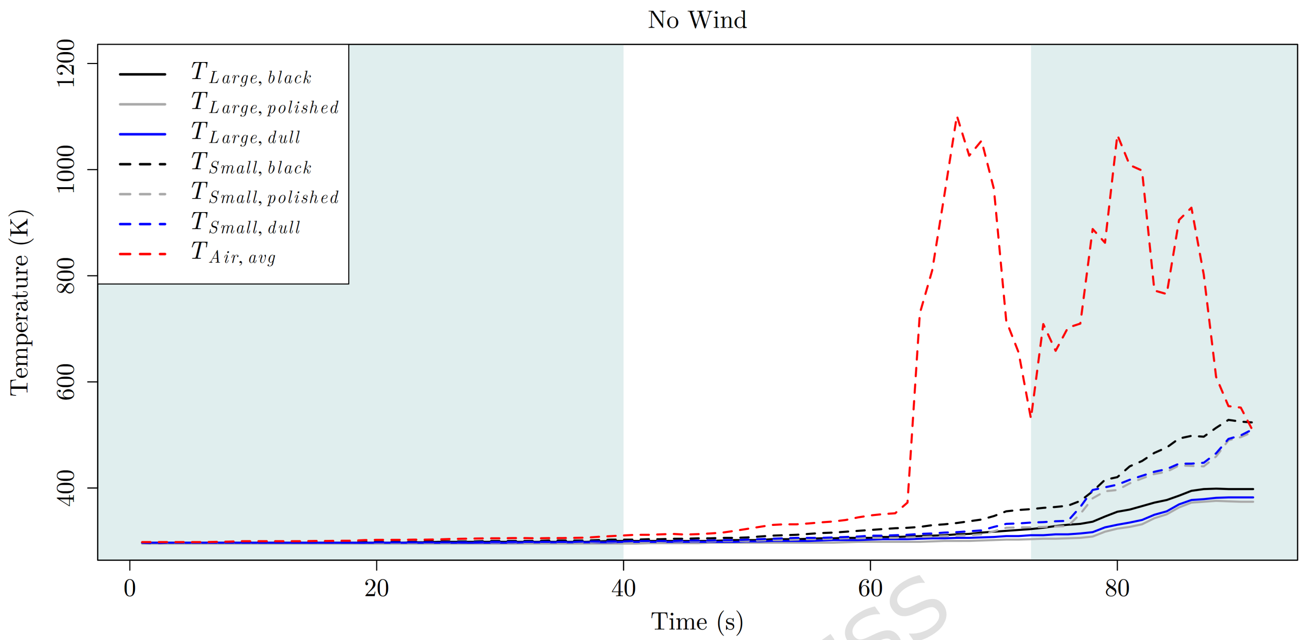

(a)

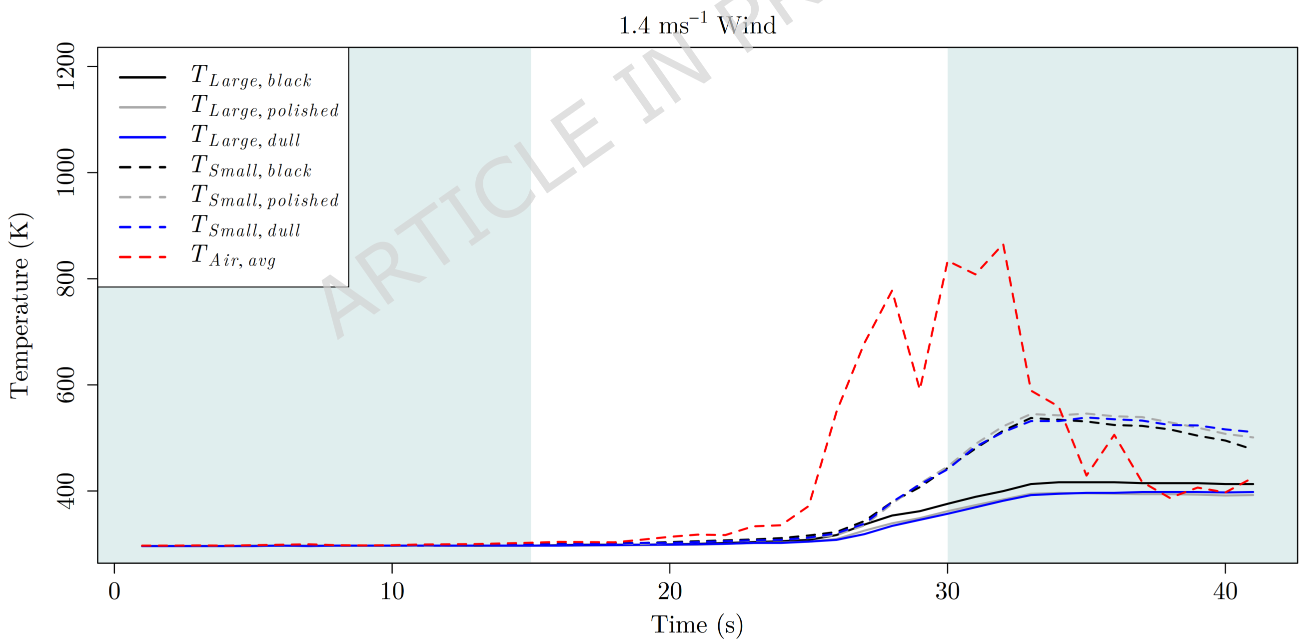

(b)

Figure 6. Temperature measurements in laboratory experiments. Both the small and larger probes are shown in (a) no wind and (b) 1.4 ms^{-1} wind scenarios. In both plots $T_{Air,avg}$ is the average air temperature from the two fine wire thermocouples. Shading on the background of the plot indicates time periods where data is not discussed in the analysis below, but is shown here for completeness.

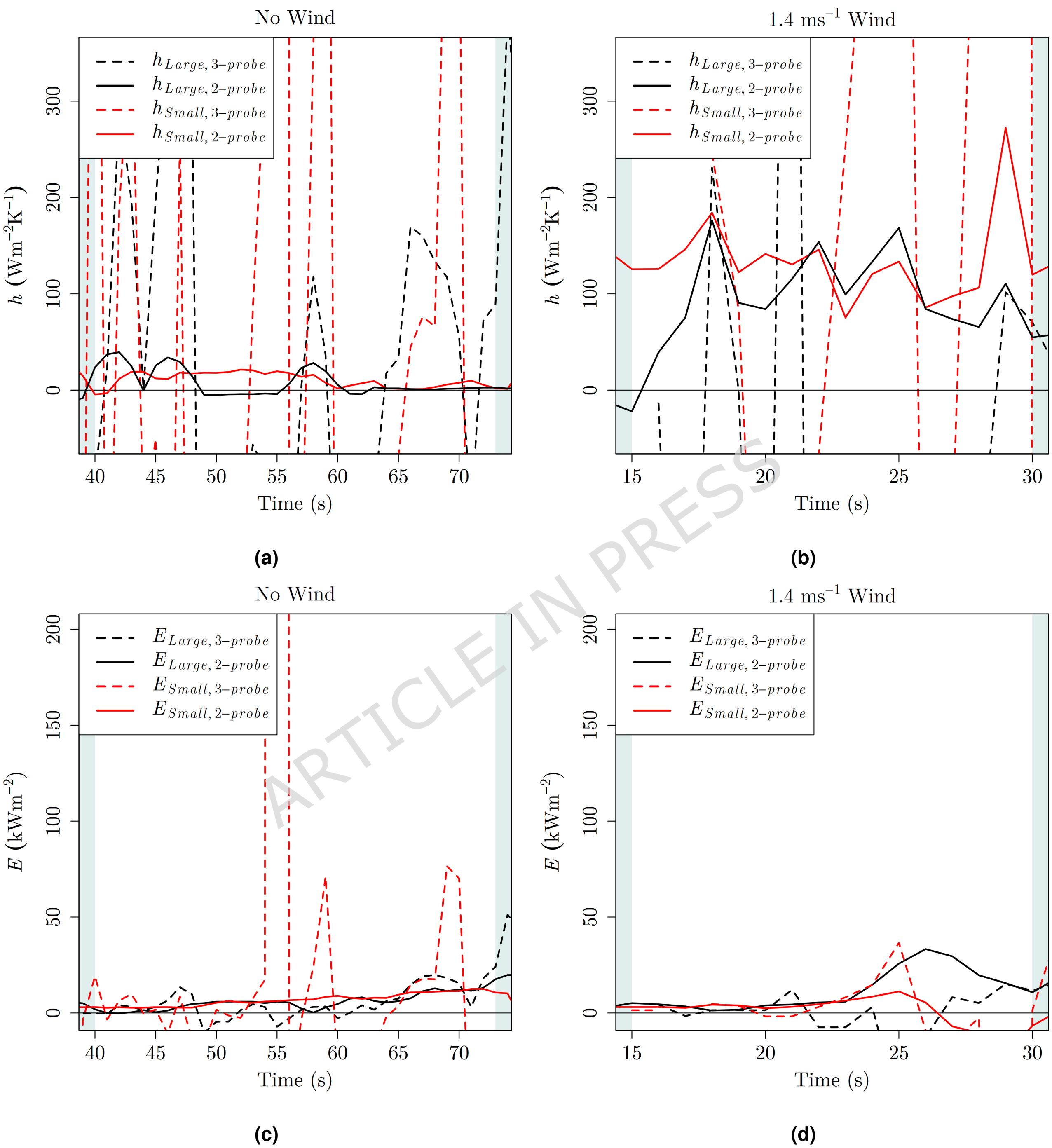

Figure 7. Calculated convective heat transfer coefficient, h, and incident radiation, E in laboratory experiments for both 2- and 3-probe systems. h is plotted in (a) no wind and (b) 1.4 ms^{-1} scenarios. E is plotted in (c) no wind and (d) 1.4 ms^{-1} scenarios.

values of convective heat transfer in several instances. At these times, there is no measured change in the temperature of the polished probe, i.e., $\frac{dT_2}{dt} = 0$, and thus the second term in the numerator of Equation 17, $D_2\varepsilon_1$, reduces to $\sigma\varepsilon_2 T_2^4 \varepsilon_1$. This results in a change of sign in the numerator and a slightly negative value of h. The small probes are more consistent, remaining below 30 $\text{Wm}^{-2}\text{K}^{-1}$ and generally near zero, which is reasonable since there is little air movement. Initially the it's value is slightly below zero, however, the temperature difference between the air and the probes is very small, such that the calculation of h when $T_i \approx T_{air}$ is irrelevant.

In the wind scenario, the mean (peak) heat transfer coefficient is 133 (272) $\text{Wm}^{-2}\text{K}^{-1}$ in the smaller system, and 93 (176) $\text{Wm}^{-2}\text{K}^{-1}$ in the larger 2-probe system. If all else remains the same with respect to Equation 8, we expect $h_S \approx 1.45 h_L$, which is remarkably close to the observed value of 1.44 using the means. The relatively consistent mean value for the heat transfer coefficient in the small 2-probe system (133 $\text{Wm}^{-2}\text{K}^{-1}$) is larger than the calculated coefficient of 102 $\text{Wm}^{-2}\text{K}^{-1}$ using Equation 8 when winds are 1.4 ms^{-1}. However, values of h in the wind scenario are expected to be greater than those estimated using pre-fire winds since fire-induced winds are often greater than ambient. Similar, but larger-scale experiments in wooden cribs[17] report in-fire winds approximately 7× the ambient wind based on video observations. Given the scale differences between the experiment presented here and those by[17], we expect winds occurring before arrival of flames in our experiments to be less than 7× the pre-fire ambient wind. For illustration purposes, we obtain a convective heat transfer coefficient of 244 $\text{Wm}^{-2}\text{K}^{-1}$ using the small probe diameter and 1000 K if we increase the wind speed to 7 ×. Other studies[63] have noted local wind speed increases approximately 3 × ambient over grass fire at 2 m AGL. Using Equation 8 and the mean heat transfer coefficient, we estimate the in-fire wind speeds to be 2.668 ms^{-1}, which is 1.9 times ambient.

The incident radiation, E, in the no wind scenario (Figure 7c) remains low for both the large and small 2-probe systems, until the flame front approaches. However, there is a very slight dip below 0 in several occasions in the larger probe system (minimum -0.57kWm^{-2}), which could be attributed to minor errors in emissivity, or other assumed values. E in the smaller 2-probe system is steadier and remains low prior to flaming. Peak incident radiant heat prior to flame arrival for small and larger 2-probe systems are 13 and 17 kWm^{-2}, respectively, which is within the range of overall peak values measured in pine litter experiments[25]. We note that our estimated $\alpha\sigma\delta$ value, a dimensionless parameter used in porous litter beds that is correlated to spread rates[64], is nearly double the highest value reported by Campbell-Lochrie *et al.*[25], although our fuel load is within the range of fuel loads tested in their study. Incident radiation calculated by both the small and large syste,s should be identical as the radiant energy per-unit-time per-unit-area does not depend on the size of the probes. Therefore, the observed similarities are encouraging.

Incident radiation for both sets of 2-probe systems is steady near 3.5 kWm^{-2} in the first half of the wind experiment (Figure 7d). At approximately 23 s, the larger system indicates a rise in radiation for 4 s increasing approximately 5.5 ×, which is contrasted by a slight rise in the smaller probes, with a peak at 25 s. Negative values of E are observed in the small probes during the wind scenario from 27 s to 29 s coinciding with a "crossover" point in probe temperatures, i.e., the time evolution of the polished probe temperature approaches and rises above the black probe temperature. If we return to Equation 18 and assume $T_{black} \approx T_{polished} = T$, we arrive at the condition where $E < 0$ using the definition of D_i:

$$A\sigma T^4 \left(\varepsilon_{black} - \varepsilon_{polished}\right) < c_p m \left(\frac{\partial T_{polished}}{\partial t} - \frac{\partial T_{black}}{\partial t}\right). \tag{21}$$

This implies that the difference in emitted radiation in the black and polished probes is less than the difference in internal energy change between the polished and black probes. This can occur when convective heat transfer is strong and incident radiation is weak, so small errors in the system calculation result in the incident radiation falling below zero to compensate for either an overestimate in convective heat transfer, or an error in internal energy change. It is interesting to note that the same behaviour is not observed in the larger probes indicating further investigation is required to determine the effects of probe size and relevant time scales associated with the fire.

Examining possible sources of error (see Supplementary Material), we find that differences in results over reasonable ranges of emissivity (0.88–0.98 and 0.05—0.2 for black and polished probes, respectively), compared to baseline values, are generally less than 22 % in h where wind is present and convective heat exchange is significant. Percent variations in calculated E are generally less than h, except in this case, where we briefly note an erroneous negative incident radiation flux. However, while E contains possible errors due to emissivity variation, the impact is not large enough to explain the anomalous values. Furthermore, an examination possible errors due to 5% temperature measurement indicates that impacts on h and E in laboratory experiments are generally less than 10% when averaged, with the largest errors occurring in the convective heat transfer coefficient (up to 94%) when temperature differences are small and convective heat transfer is weak. This again does not account for anomalous values in E. Given the sensitivity of the solutions to temperature cross overs occurring when denominators are small, a confidence flag should be reported with the dataset, or data should be skipped or downweighted to avoid instabilities or anomalous solutions. While we recognize that this is a current limitation of the sensor in a unique scenario, we leave corrections of this limitation for future work.

Following our approach in the case of field experiments above, we only present the energy budget for the 2-probe systems. As shown in Figures 8a and 8b for the large and small systems with no wind, respectively, the overall energy budget shows very little energy transfer to the probes via both convective and radiative heating. The black probe in both sizes generally absorbs more thermal radiation than the polished probes, as expected. In both cases, convective heating is near 0, with the exception of the smaller probes immediately before flame arrival between 67 s and 72 s. While air temperatures are elevated after 60 s, little air movement prevents significant heat transfer between the gas and solid surface. We also recognize that increasing local air temperature around the probes would lag by several seconds compared with the reported air temperatures since the probes fine wire thermocouples are separated by 1.5–2 cm. Furthermore, the fact that probe temperatures do not rise appreciably until flames are in direct contact with the probes reveals that in still conditions with sub-meter flame lengths, the sensors may not be able to determine heat transfer as well as other methods in a completely still scenario where heating is almost entirely radiative until direct contact with flame. Conversely, the wind scenario (Figures 8c and 8d for the large and small probes, respectively) shows some radiative heating prior to arrival of the flames, but heating is dominated by convection pre-flame contact in both cases. Other studies report a correlation during pre-heating between the role of convective heat transfer with increasing wind[28], or observe strong convective heat pulses when fire behaviour is largely wind driven[23,33,39]. These trends, however, contrast those found by Butler *et al.*[65], where radiation magnitudes were generally double that of convective heat during wind driven fire experiments. The significant difference in scale of the laboratory experiments[65] could play a role in the differences from the results here since radiative energy emitted by the fire is related to fuel consumption[33,66]. Their[65] fuel beds were pine straw, 3 m × 24 m, with fuel loads nearly 3 times our grass fuel loads. This difference could also be partially attributed to the fact that the sensor packages in Butler *et al.* included heat transfer to a flat plate. It is important to remember that convective heat transfer to a flat plate is different than that received by a probe (or fine fuels), and so direct comparison to the studies discussed above and their findings related to convective heat transfer and the probe results here are not possible. Instead, we highlight general trend comparisons and estimated wind speeds which are tied to convective heat transfer, recognizing that further testing and validation is required and will be reported in future work.

Conclusion

This study looked at developing and testing a cost effective, simple heat transfer sensor for wildfire applications. Performance of the proposed system was evaluated under both field tests and lab experiments over a range of environmental conditions, including high-intensity crown fire, as well as lower intensity grass fires in both calm and wind-driven scenarios.

The result of our field tests revealed that the heat transfer system configuration with 3-probes is unable to resolve the rapid changes in convective heat transfer and produces unphysical results. However, when coupled with air temperature measurements, the sensor is providing physically realistic results when compared with literature and plausible scenarios. The measured incident radiation, convective heat transfer coefficient, and estimated wind speeds are within the ranges of those observed by other field studies. Initial measurements found increasing radiative heat transfer with decreasing distance to the flame front, which is consistent with expectations. Furthermore, turbulence induced bursts of convective heating and cooling ahead of the front were also documented.

Laboratory tests indicate similar performance in calm and wind-driven tests. In these tests, we find the smaller probes increase sensitivity of the sensor. Radiant heating increases as the flame approaches and estimated in-fire wind speeds are nearly double ambient wind speeds, which is consistent with other studies. However, these simple tests reveal potential challenges in cases where convective heat transfer is strong and incident radiation is weak indicating small errors may be present. in estimated values of emissivity. While laboratory studies are valuable to test proof of concept here, the smaller probe system still requires rigorous testing in experimental or prescribe fire alongside established sensor packages to ensure consistent and accurate results in highly dynamic environments.

Funding

Internal funding was provided by Natural Resources Canada through the Wildfire Resilient Futures Initiative. There is no external funding source.

Author contributions statement

R.L., S.G., and J.O. conceptualized and patented the sensor. A.H. and R.L. provided supervision. R.L., S.G., J.O., D.K., G.M., A.H. contributed to field experimental design. D.K. acquired funding. G.M. conceived laboratory experimental design. G.M. conducted all experiments, performed the analysis, and produced the figures. G.M. wrote the original manuscript with assistance from R.L. and D.T. All authors reviewed the manuscript.

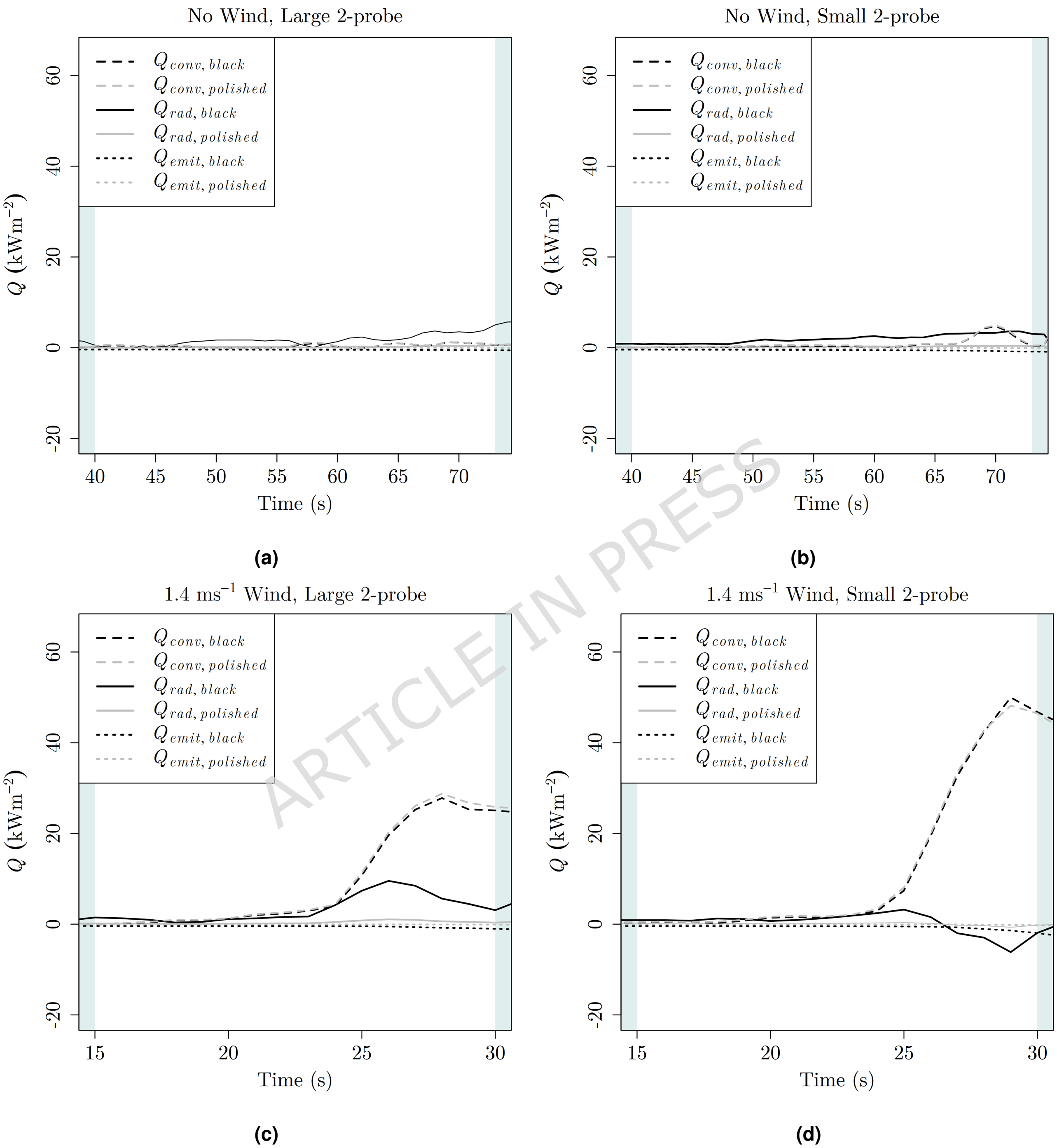

Figure 8. Energy budget calculation the 2-probe systems in laboratory experiments. The large probes are plotted in (a) no wind and (c) 1.4 ms^{-1} wind laboratory experiments and the small probes in (b) no wind and (d) 1.4 ms^{-1} .

Data Availability

All data analyzed during this study are included in this published article (and its Supplementary Information files).

Acknowledgements

We would like to thank Westley Steed and the Government of the Northwest Territories Environment and Climate Change for organizing and conducting the experimental fire. We also thank Greg Baxter with FPInnovations and Kimberly Morrison and Stefana Dranga at the Pacific Forestry Centre for their assistance with equipment and data collection.

References

1. Byram, G. M. Combustinon of Forest Fuels. In Davis, K. P. (ed.) *Forest Fire: Control and Use*, 61–89 (McGraw-Hill, New York, NY, 1959).
2. Finney, M. A., Cohen, J. D., McAllister, S. S. & Jolly, W. M. On the need for a theory of wildland fire spread. *Int. J. Wildland Fire* **22**, 25, DOI: 10.1071/WF11117 (2013).
3. Prichard, S. *et al.* The Fire and Smoke Model Evaluation Experiment—A Plan for Integrated, Large Fire–Atmosphere Field Campaigns. *Atmosphere* **10**, 66, DOI: 10.3390/atmos10020066 (2019).
4. Alexander, M. E. & Cruz, M. G. Are the applications of wildland fire behaviour models getting ahead of their evaluation again? *Environ. Model. & Softw.* **41**, 65–71, DOI: 10.1016/j.envsoft.2012.11.001 (2013).
5. Cruz, M. G., Alexander, M. E. & Sullivan, A. L. Mantras of wildland fire behaviour modelling: Facts or fallacies? *Int. J. Wildland Fire* **26**, 973, DOI: 10.1071/WF17097 (2017).
6. Kremens, R. L., Smith, A. M. S. & Dickinson, M. B. Fire Metrology: Current and Future Directions in Physics-Based Measurements. *Fire Ecol.* **6**, 13–35, DOI: 10.4996/fireecology.0601013 (2010).
7. Sullivan, A. L. Inside the Inferno: Fundamental Processes of Wildland Fire Behaviour: Part 2: Heat Transfer and Interactions. *Curr. For. Reports* **3**, 150–171, DOI: 10.1007/s40725-017-0058-z (2017).
8. Finney, M. A., McAllister, S. S., Grumstrup, T. P. & Forthofer, J. M. *Wildland Fire Behaviour*. Dynamics, Principles and Processes (CSIRO Publishing, 2021).
9. Drysdale, D. *An Introduction to Fire Dynamics* (Wiley, Chichester, West Sussex, 2011), 3rd ed edn.
10. Fons, W. L. Analysis of fire spread in light forest fuels. *J. Agric. Res.* **72**, 93–121 (1949).
11. Mueller, E. V. *et al.* Local measurements of wildland fire dynamics in a field-scale experiment. *Combust. Flame* **194**, 452–463, DOI: 10.1016/j.combustflame.2018.05.028 (2018).
12. Cunningham, P. & Linn, R. R. Numerical simulations of grass fires using a coupled atmosphere-fire model: Dynamics of fire spread. *J. Geophys. Res. Atmospheres* **112**, 2006JD007638, DOI: 10.1029/2006JD007638 (2007).
13. Linn, R. R., Winterkamp, J. L., Weise, D. R. & Edminster, C. A numerical study of slope and fuel structure effects on coupled wildfire behaviour. *Int. J. Wildland Fire* **19**, 179, DOI: 10.1071/WF07120 (2010).
14. Finney, M. A. *et al.* Role of buoyant flame dynamics in wildfire spread. *Proc. Natl. Acad. Sci.* **112**, 9833–9838, DOI: 10.1073/pnas.1504498112 (2015).
15. Liu, N. *et al.* Upslope spread of a linear flame front over a pine needle fuel bed: The role of convection cooling. *Proc. Combust. Inst.* **35**, 2691–2698, DOI: 10.1016/j.proci.2014.05.100 (2015).
16. Cohen, J. D. & Finney, M. A. Fuel Particle Heat Transfer Part 1: Convective Cooling of Irradiated Fuel Particles. *Combust. Sci. Technol.* **195**, 3095–3121, DOI: 10.1080/00102202.2021.2019231 (2023).
17. Cohen, J. & Finney, M. Fuel Particle Heat Transfer Part 2: Radiation and Convection during Spreading Laboratory Fires. *Combust. Sci. Technol.* **195**, 3122–3147, DOI: 10.1080/00102202.2021.2019232 (2023).
18. Anderson, W. R., Catchpole, E. A. & Butler, B. W. Convective heat transfer in fire spread through fine fuel beds. *Int. J. Wildland Fire* **19**, 284, DOI: 10.1071/WF09021 (2010).
19. Butler, B. W., Jimenez, D., Forthofer, J., Shannon, K. & Sopko, P. A Portable System for Characterizing Wildland Fire Behavior. In Viegas, D. X. (ed.) *VI International Conference on Forest Fire Research*, 13 (University of Coimbra, Coimbra, Portugal, 2010).
20. Zhang, Y. & Nakamura, Y. Numerical study of instability mechanisms and scaling relation in boundary layer flame. *Combust. Flame* **280**, 114405, DOI: 10.1016/j.combustflame.2025.114405 (2025).

21. He, Q. *et al.* Experimental study on fire spread over discrete fuel bed-Part II: Combined effects of wind and packing ratio. *Fire Saf. J.* **128**, 103520, DOI: 10.1016/j.firesaf.2021.103520 (2022).

22. Dupuy, J.-L. & Maréchal, J. Slope effect on laboratory fire spread: Contribution of radiation and convection to fuel bed preheating. *Int. J. Wildland Fire* **20**, 289, DOI: 10.1071/WF09076 (2011).

23. Frankman, D., Webb, B. W. & Butler, B. W. Time-Resolved Radiation and Convection Heat Transfer in Combusting Discontinuous Fuel Beds. *Combust. Sci. Technol.* **182**, 1391–1412, DOI: 10.1080/00102202.2010.486388 (2010).

24. Morandini, F., Silvani, X., Dupuy, J.-L. & Susset, A. Fire spread across a sloping fuel bed: Flame dynamics and heat transfers. *Combust. Flame* **190**, 158–170, DOI: 10.1016/j.combustflame.2017.11.025 (2018).

25. Campbell-Lochrie, Z. *et al.* Effects of fuel bed structure on heat transfer mechanisms within and above porous fuel beds in quiescent flame spread scenarios. *Int. J. Wildland Fire* DOI: 10.1071/WF22129 (2023).

26. Yedinak, K. M., Strand, E. K., Hiers, J. K. & Varner, J. M. Embracing Complexity to Advance the Science of Wildland Fire Behavior. *Fire* **1**, 20, DOI: 10.3390/fire1020020 (2018).

27. Grumstrup, T. P., Jason, F. & A., F., Mark. Measurement of three-dimensional flow speed and direction in wildfires. In Viegas, D. X. (ed.) *Proceedings of the VII International Conference on Forest Fire Research*, 542–548, DOI: 10.14195/978-989-26-16-506_60 (Imprensa da Universidade de Coimbra, Coimbra, Portugal, 2018).

28. Morandini, F. & Silvani, X. Experimental investigation of the physical mechanisms governing the spread of wildfires. *Int. J. Wildland Fire* **19**, 570, DOI: 10.1071/WF08113 (2010).

29. Silvani, X. & Morandini, F. Fire spread experiments in the field: Temperature and heat fluxes measurements. *Fire Saf. J.* **44**, 279–285, DOI: 10.1016/j.firesaf.2008.06.004 (2009).

30. Butler, B. W. *et al.* Measurements of radiant emissive power and temperatures in crown fires. *Can. J. For. Res.* **34**, 1577–1587, DOI: 10.1139/x04-060 (2004).

31. Butler, B. *et al.* Observations of energy transport and rate of spreads from low-intensity fires in longleaf pine habitat – RxCADRE 2012. *Int. J. Wildland Fire* **25**, 76, DOI: 10.1071/WF14154 (2016).

32. Morandini, F., Toulouse, T., Silvani, X., Pieri, A. & Rossi, L. Image-Based Diagnostic System for the Measurement of Flame Properties and Radiation. *Fire Technol.* **55**, 2443–2463, DOI: 10.1007/s10694-019-00873-1 (2019).

33. Frankman, D. *et al.* Measurements of convective and radiative heating in wildland fires. *Int. J. Wildland Fire* **22**, 157, DOI: 10.1071/WF11097 (2013).

34. Tihay, V., Morandini, F., Santoni, P.-A., Perez-Ramirez, Y. & Barboni, T. Combustion of forest litters under slope conditions: Burning rate, heat release rate, convective and radiant fractions for different loads. *Combust. Flame* **161**, 3237–3248, DOI: 10.1016/j.combustflame.2014.06.003 (2014).

35. Lentile, L. B. *et al.* Remote sensing techniques to assess active fire characteristics and post-fire effects. *Int. J. Wildland Fire* **15**, 319, DOI: 10.1071/WF05097 (2006).

36. Johnston, J. M., Wooster, M. J. & Lynham, T. J. Experimental confirmation of the MWIR and LWIR grey body assumption for vegetation fire flame emissivity. *Int. J. Wildland Fire* **23**, 463, DOI: 10.1071/WF12197 (2014).

37. Freeborn, P. H. *et al.* Relationships between energy release, fuel mass loss, and trace gas and aerosol emissions during laboratory biomass fires. *J. Geophys. Res. Atmospheres* **113**, 2007JD008679, DOI: 10.1029/2007JD008679 (2008).

38. Filkov, A. I. *et al.* A review of thermal exposure and fire spread mechanisms in large outdoor fires and the built environment. *Fire Saf. J.* **140**, 103871, DOI: 10.1016/j.firesaf.2023.103871 (2023).

39. Frankman, D., Webb, B. W., Butler, B. W., Jimenez, D. & Harrington, M. The effect of sampling rate on interpretation of the temporal characteristics of radiative and convective heating in wildland flames. *Int. J. Wildland Fire* **22**, 168, DOI: 10.1071/WF12034 (2013).

40. Cruz, M. G., Butler, B. W., Viegas, D. X. & Palheiro, P. Characterization of flame radiosity in shrubland fires. *Combust. Flame* **158**, 1970–1976, DOI: 10.1016/j.combustflame.2011.03.002 (2011).

41. Wickström, U., Anderson, J. & Sjöström, J. Measuring incident heat flux and adiabatic surface temperature with plate thermometers in ambient and high temperatures. *Fire Mater.* **43**, 51–56, DOI: 10.1002/fam.2667 (2019).

42. Wickström, U. The plate thermometer - a simple instrument for reaching harmonized fire resistance tests. *Fire Technol.* **30**, 195–208, DOI: 10.1007/BF01040002 (1994).

43. McClure, A. B. *et al.* Estimating heat tolerance of buds in southeastern US trees in fire-prone forests. *Fire Ecol.* **18**, 32, DOI: 10.1186/s42408-022-00160-5 (2022).

44. Dickinson, M. B. *et al.* The Wildland Fire Heat Budget—Using Bi-Directional Probes to Measure Sensible Heat Flux and Energy in Surface Fires. *Sensors* **21**, 2135, DOI: 10.3390/s21062135 (2021).

45. Linn, R. R., Goodrick, S. & O'Brien, J. J. Forest Fire Fuel Heat Transfer Sensor (May 7, 2019).

46. Incropera, F. P., DeWitt, D. P., Bergman, T. L. & Lavine, A. S. *Fundamentals of Heat and Mass Transfer* (John Wiley, Hoboken, NJ, 2007), 6th ed edn.

47. Cunningham, P., Goodrick, S. L., Hussaini, M. Y. & Linn, R. R. Coherent vortical structures in numerical simulations of buoyant plumes from wildland fires. *Int. J. Wildland Fire* **14**, 61, DOI: 10.1071/WF04044 (2005).

48. Fritschen, L. J. & Gay, L. W. *Environmental Instrumentation*. Springer Advanced Texts in Life Sciences (Springer New York, New York, NY, 1979).

49. Wood, W. D., Deem, H. W. & Lucks, C. F. Thermal Radiative Properties of Selected Materials.

50. FLIR Systems, Inc. Reference documetation Thermography. https://support.flir.com/DSDownload/Assets/T810442-en-US_A4.pdf (2019).

51. Emissivity Coefficients of Common Materials: Data & Reference Guide. https://www.engineeringtoolbox.com/emissivity-coefficients-d_447.html.

52. Henninger, H. Solar Absorptance and Thermal Emittance of Some Common Spacecraft Thermal-Control Coatings.

53. Government of Northwest Territories,Environment and Climate Change. Fort Providence Wildfire Experimental Site. https://www.gov.nt.ca/ecc/en/services/wildfire-operations/fort-providence-wildfire-experimental-site.

54. Stocks, B. J., Alexander, M. E. & Lanoville, R. A. Overview of the International Crown Fire Modelling Experiment (ICFME). *Can. J. For. Res.* **34**, 1543–1547, DOI: 10.1139/x04-905 (2004).

55. Van Wagner, C. E. *Development and Structure of the Canadian Forest Fire Weather Index System*. No. 35 in Forestry Technical Report (Minister of Supply and Services Canada, Ottawa, 1987).

56. Walker, J. D. & Stocks, B. J. Thermocouple errors in forest fire research. *Fire Technol.* **4**, 59–62, DOI: 10.1007/BF02588607 (1968).

57. Leventon, I. T., Korver, K. T. & Stoliarov, S. I. A generalized model of flame to surface heat feedback for laminar wall flames. *Combust. Flame* **179**, 338–353, DOI: 10.1016/j.combustflame.2017.02.007 (2017).

58. Clark, T. L., Radke, L., Coen, J. & Middleton, D. Analysis of Small-Scale Convective Dynamics in a Crown Fire Using Infrared Video Camera Imagery. *J. Appl. Meteorol.* **38**, 1401–1420, DOI: 10.1175/1520-0450(1999)038<1401:AOSSCD>2.0.CO;2 (1999).

59. Coen, J., Mahalingam, S. & Daily, J. Infrared Imagery of Crown-Fire Dynamics during FROSTFIRE. *J. Appl. Meteorol.* **43**, 1241–1259, DOI: 10.1175/1520-0450(2004)043<1241:IIOCDD>2.0.CO;2 (2004).

60. Monod, B., Collin, A., Parent, G. & Boulet, P. Infrared radiative properties of vegetation involved in forest fires. *Fire Saf. J.* **44**, 88–95, DOI: 10.1016/j.firesaf.2008.03.009 (2009).

61. Acem, Z., Parent, G., Monod, B., Jeandel, G. & Boulet, P. Experimental study in the infrared of the radiative properties of pine needles. *Exp. Therm. Fluid Sci.* **34**, 893–899, DOI: 10.1016/j.expthermflusci.2010.02.003 (2010).

62. Butler, B., Parsons, R. & Mell, W. Recent Findings Relating to Firefighter Safety Zones. In *Proceedings of the Large Wildland Fires Conference; May 19-23, 2014; Missoula, MT* (2015).

63. Clements, C. *et al.* Observing the dynamics of wildland grass fires: FireFlux—a field validation experiment. *Bull. The Am. Meteorol. Soc.* **88**, DOI: 10.1175/BAMS-88-9-1369 (2007).

64. Campbell-Lochrie, Z. *et al.* Investigation of the role of bulk properties and in-bed structure in the flow regime of buoyancy-dominated flame spread in porous fuel beds. *Fire Saf. J.* **120**, 103035, DOI: 10.1016/j.firesaf.2020.103035 (2021).

65. Butler, B. *et al.* Exploring fire response to high wind speeds: Fire rate of spread, energy release and flame residence time from fires burned in pine needle beds under winds up to 27 ms-1. *Int. J. Wildland Fire* **29**, 81, DOI: 10.1071/WF18216 (2020).

66. Wooster, M. J., Roberts, G., Perry, G. L. W. & Kaufman, Y. J. Retrieval of biomass combustion rates and totals from fire radiative power observations: FRP derivation and calibration relationships between biomass consumption and fire radiative energy release. *J. Geophys. Res. Atmospheres* **110**, 2005JD006318, DOI: 10.1029/2005JD006318 (2005).